AN UNUSUAL STELLAR DEATH ON CHRISTMAS DAY

C. C. Thöne [1,2], A. de Ugarte Postigo[3], C. L. Fryer[4], K. L. Page[5], J. Gorosabel[1], D. A. Perley[6], C. Kouveliotou[7], H. T. Janka[8], M. A. Aloy[9], P. Mimica [9], J. L. Racusin [10], H. Krimm [10,11,12], J. Cummings [10], S. R. Oates[13], S. T. Holland[10,11,12], M. H. Siegel[14], M. De Pasquale[13], E. Sonbas[10,11,15], M. Im[16], W.-K. Park[16], D. A. Kann[17], S. Guziy[1], L. Hernández García[1], K. Bundy[6], A. J. Castro-Tirado[1], C. Choi[16], H. Jeong[18], H. Korhonen[19], P. Kubanek[1,20], J. Lim[21], A. Llorente[22], A. Moskvitin[23],T. Muñoz Darias[24], S. Pak[18], I. Parrish[6]

Draft April 2011

ABSTRACT

Massive stars can end their lives in many different ways. Long Gamma-Ray Bursts (GRBs) are the most dramatic examples, releasing ultra-relativistic ejecta that produce non-thermal emission when interacting with the surrounding medium (Zhang et al. 2004). Usually, those events are accompanied by a supernova (SN) (Woosley et al. 2006). In a few low-redshift GRB-SNe we could observe the actual breakout of the shock front from the surface of the star (Campana et al. 2006). Here we present GRB 101225A, a very peculiar event at a distance of 1.6 Gpc. A bright X-ray transient with a thermal component and an unusual optical counterpart followed an exceptionally long γ-ray event detected by the *Swift* satellite. During the first 10 days, the optical emission evolved as an expanding, cooling blackbody (BB) with a large initial radius, after which a faint SN was observed. The absence of a normal GRB afterglow implies that some dense material, likely ejected by the progenitor star, completely thermalized the high-energy emission. A possible progenitor is a helium star/neutron star binary which underwent a common envelope phase, expelling its hydrogen envelope prior to the explosion. The final merging process created a GRB-like event where we observe the shock breakout of the secondary star before the high-energy emission gets thermalized in the collision with the previously expelled shell, until finally the emission from the SN itself takes over. GRB 101225A defines a new, rare type of blackbody-dominated GRB which explodes in a dense environment created by the progenitor system itself.

Subject headings: Gamma-rays: Bursts: Individual: GRB 101225

Based on observations collected at CAHA/Calar Alto, GTC/La Palma under proposal 105-GTC34/10B, the Liverpool Telescope at ORM/La Palma, the McDonald Observatory at the University of Texas at Austin, Gemini-North and Keck on Big Island/Hawaii.

cthoene@iaa.es
[1] IAA - CSIC, Glorieta de la Astronomía s/n, 18008 Granada, Spain
[2] Niels Bohr International Academy, Niels Bohr Institute, Blegdamsvej 17, 2100 Copenhagen, Denmark
[3] Dark Cosmology Centre, Niels Bohr Institute, Univ. of Copenhagen, Juliane Maries Vej 30, 2100 Copenhagen, Denmark
[4] Los Alamos National Laboratory, MS D409, CCS-2, Los Alamos, NM 87545, USA
[5] Department of Physics & Astronomy, Univ. of Leicester, University Road, Leicester LE1 7RH, UK
[6] UC Berkeley, Astronomy Department, 601 Campbell Hall, Berkeley CA 94720, USA
[7] NASA, Marshall Space Flight Centre, NSSTC, 320 Sparkman Drive, Huntsville, AL 35805, USA
[8] Max-Planck-Institut für Astrophysik, Karl-Schwarzschild-Str. 1, 85748 Garching, Germany
[9] Departamento de Astronomia y Astrofisica, Universidad de Valencia, 46100 Burjassot, Spain
[10] NASA, Goddard Space Flight Center, Greenbelt, MD 20771, USA
[11] Universities Space Research Association, 10211 Wincopin Circle, Suite 500, Columbia, MD 21044-3432, USA
[12] Center for Research and Exploration in Space Science and Technology (CRESST)
[13] Mullard Space Science Laboratory, Holmbury St. Mary, Dorking, Surrey RH5 6NT, UK
[14] Dep. of Astronomy & Astrophysics, Pennsylvania State Univ., 104 Davey Laboratory, University Park, PA 16802, USA
[15] University of Adıyaman, Department of Physics, 02040 Adıyaman, Turkey
[16] Center for the Exploration of the Origin of the Universe, Dept. of Physics & Astronomy, Seoul National University, 56-1 San, Shillim-dong, Kwanak-gu, Seoul, Korea
[17] Thüringer Landessternwarte Tautenburg, Sternwarte 5, 07778 Tautenburg, Germany
[18] School of Space Research, Kyung Hee University, 1 Seocheon-dong, Giheung-gu, Yongin-si, Gyeonggi-do 446-701, Korea
[19] Finnish Centre for Astronomy with ESO (FINCA), University of Turku, Väisäläntie 20, 21500 Piikkiö, Finland
[20] Institute of Physics, Na Slovance 2, 180 00, Prague 8, Czech Republic
[21] Dept. of Astronomy and Space Science, Kyung Hee University, 1 Seocheon-dong, Giheung-gu, Yongin-si, Gyeonggi-do 446-701, Korea
[22] Herschel Science Operations Centre, INSA, ESAC, Villafranca del Castillo, PO Box 50727, I-28080 Madrid, Spain
[23] Special Astrophysical Observatory of the Russian Academy of Sciences, Nizhnij Arkhyz 369167, Russia
[24] INAF - Osservatorio Astronomico di Brera, Via E. Bianchi 46, 23807 Merate, Italy

1. INTRODUCTION

On Dec. 25, 2010, 18:37:45 UT (T_0), the BAT (15-350 keV) instrument onboard the *Swift* satellite detected GRB 101225A in an image trigger. It had a soft γ-ray spectrum and one of the longest durations ($T_{90} > 2000$ s, the time in which 90% of the energy is released) of any burst observed by *Swift* (Sakamoto et al. 2010). Despite its low fluence, the long duration makes its high-energy output similar to those of other long-duration GRBs.

At T-T_0 = 1400 s after the trigger, XRT, the X-ray telescope onboard *Swift*, slewed to the position and detected a bright X-ray counterpart detected up to 2 days after the burst. An optical counterpart was found by the Nordic Optical Telescope (NOT) at 1.54 h after the BAT trigger (Xu et al. 2010a) and followed up both with UVOT on-board *Swift* and several optical telescopes in different ultraviolet, optical and infrared broad-band filters from 0.38 h to 2 months after the event (see Appendix). No counterpart in radio frequencies was detected (Frail et al. 2011; Zauderer et al. 2011).

2. OBSERVATIONS

The most remarkable aspect of GRB 101225A is the spectral energy distribution (SED) and its evolution. The X-ray SED is best modeled with a combination of an absorbed power-law and a BB up to 8 ks, after which the signal to noise is too low to disentangle the two components. The contribution from the BB is around 20% of the total flux and the temperature of the BB is $1-1.5$ keV with no significant temporal evolution. The UV/optical/NIR (UVOIR) SED (see Fig. 1) can be modeled with a cooling and expanding BB model up to 10 days after the event. The SEDs of GRBs usually follow a power-law due to synchrotron emission created in the external shocks between the GRB jet and the interstellar medium (e.g., Zhang et al. 2004), which is completely absent for GRB 101225A.

At 10 days, an additional component becomes evident in the UVOIR SED accompanied with a flattening in the lightcurve (see Fig. 2). Both the spectrum and lightcurve are well reproduced with the Type Ic SN 1998bw (connected to GRB 090428 and used as the classic broad-lined Ic GRB-SN template) (Galama et al. 1998) at a redshift of z=0.32 stretched by a factor of 1.25 in time and with 1/12th of the luminosity of SN 1998bw (for a discussion on the redshift determination, see appendix). At this distance, the initial expansion velocity of the UVOIR BB is 90,000 km/s slightly higher than typical SN ejecta. At z =0.32 the SN has an absolute peak magnitude of only $M_V = -16.7$ mag. This would make it the faintest SN associated with a long GRB ever detected, 2.3 mag fainter than SN 19988bw/GRB 980425, and significantly fainter than the GRB 040924 SN, (Soderberg et al. 2006; Wiersema et al. 2008). In contrast, the isotropic-equivalent energy release at z=0.32 is $> 1.4 \times 10^{51}$ erg in γ-rays, comparable to the total energy release of other long-duration GRBs and more luminous than a number of other low-redshift GRBs connected to SNe (Kann et al. 2010).

An optical spectrum taken 2 nights after the burst does not show any obvious absorption or emission features (for a plot of the spectrum see SI). The continuum can be fit with a power law with $F_\nu \propto \nu^{0.9}$, consistent with being on the Rayleigh-Jeans tail of the BB emission. The absence of characteristic SN lines at 2 d post-burst is not surprising, in particular considering the late peak of the SN associated with GRB 101225A. The absence of emission lines from the host galaxy indicates that it must be rather faint (see appendix). Pre-imaging of the field from the 3.5m CFHT (Richardson et al. 2011) revealed no source at the position of GRB 101225A down to a 3σ limit of $i' > 26.8$ mag (see appendix). There is a marginal (2σ) detection of an underlying source at $g' = 27.2$ mag. If this is the host galaxy at $z = 0.32$, its absolute magnitude would be $M_{\rm abs} = -13.7$ mag, ~ 2 mag fainter than the faintest GRB host galaxy detected, the host of XRF 060218 (e.g., (Wiersema et al. 2007)).

3. RESULTS FROM THE BLACK-BODY EVOLUTION

An important clue to the origin of this event comes from the modeling of the BB component at different wavelengths. The BB component in X-rays has a radius of $\sim 2 \times 10^{11}$ cm ($1\,R_\odot$) and a temperature of ~ 1 keV (10^7 K) at 0.07 d. The UVOIR BB starts with a radius of 2×10^{14} cm and a temperature of 8.5×10^4 K at the same time with an initial expansion velocity of 90,000 km s^{-1}. As shown in Fig. 3, the UVOIR BB evolution is inconsistent with the radius and temperatures of the X-ray BB component. Therefore, the emission in these two bands must stem from different processes and regions.

A BB component in X-rays had been suggested for XRF (X-ray flash) 060218/SN 2006aj (Campana et al. 2006), XRF 100316D/SN 2010dh (Starling et al. 2011) and GRB 090618 (K. Page et al. in prep.), all GRBs associated with Type Ic SNe, this component was attributed to the shock breakout from the star or the dense circumstellar wind. A shock breakout was also proposed as the origin of the X-ray emission observed in XRO (X-ray outburst) 080109/SN 2008D, a Type Ib SN in NGC 2770 (Soderberg et al. 2008). However, it showed no thermal component in the X-rays due to comptonization of the BB and was not associated with a GRB. Both XRF 060218/SN 2006aj and XRO 080109/SN 2008D had a thermal component in the optical over the first few days (see appendix). For XRO 080109/SN 2008D, the radius and temperature evolution is steeper than for GRB 101225A, which makes the UVOIR BB emission consistent with the expanding and cooling BB from the shock breakout. The UVOIR BB of XRF 060218/SN 2006aj is similar in radius and evolution to GRB 101225A while the radius inferred from X-rays is much larger (about 20 $R_\odot$). Despite the large initial radius of the X-ray thermal component, which was attributed to the shock breakout from the wind of the progenitor, the UVOIR BB emission cannot be ascribed to the continuation of the shock front into the ISM from the initial breakout.

4. INTERPRETATION

To explain the nature of this unusual event, we need to explain four different emission processes: 1) The prompt, very long high-energy emission. 2) The thermal component observed in X-rays with a small radius of $\sim 1\,R_\odot$. 3) The afterglow of the GRB which is fully described by an expanding, cooling BB with an initial radius of ~ 30 AU, which starts simultaneously with the second orbit of the X-ray observations. And 4) a late, faint SN emerging at around 10 d. The large radius of the UVOIR BB

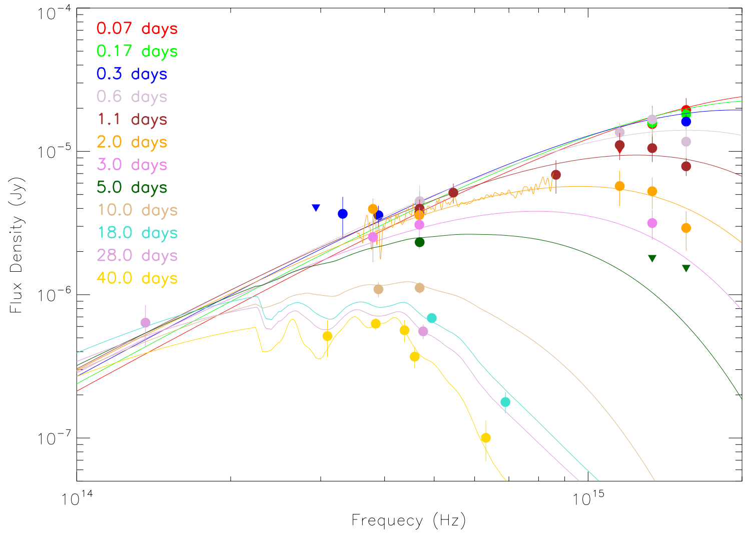

FIG. 1.— The spectral energy distribution (SED) of the UV/optical/NIR (UVOIR) counterpart of GRB 101225A at different epochs after the explosion. Filled circles are detections, triangles mark upper limits. Until 10 days, the SED is modeled with a simple BB, the last 3 epochs were modeled with an evolving SN Type Ic, similar to SN 1998bw associated with GRB 980425. The orange line on top of the BB model at 2.0 days shows our flux-calibrated spectrum taken with the OSIRIS/GTC.

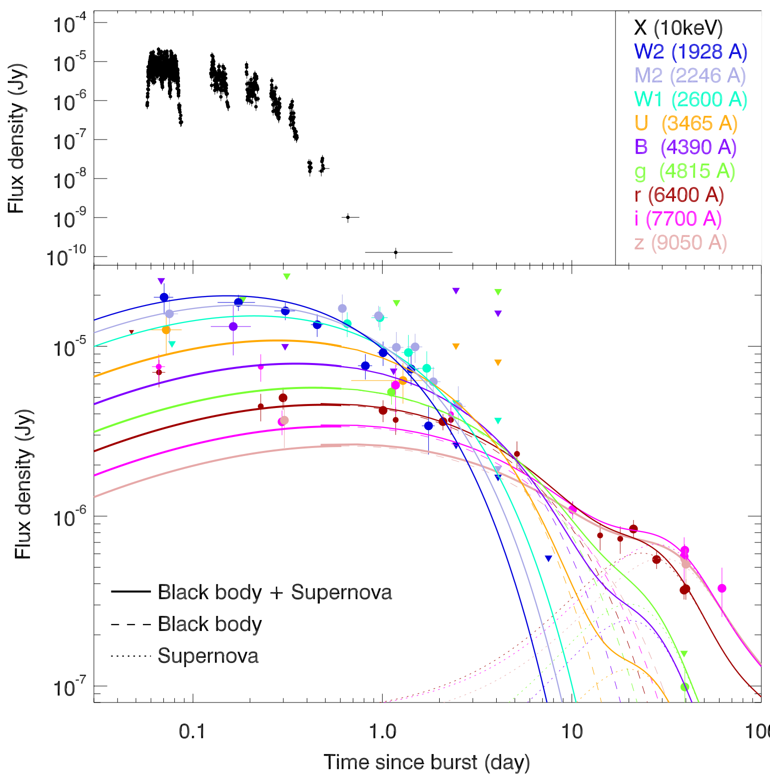

FIG. 2.— Light curves of GRB 101225A in X-rays (black, top panel) and UVOIR (bottom panel). The over plotted lines are the evolution of the light curves in the different bands as estimated from the temporal evolution of the BB. Observations started almost simultaneously in X-rays and optical/UV wavelengths. The X-rays reached a peak flux of 4.34×10^{-9} erg cm^{-2} s^{-1}. After an initial shallow decay of slope $t^{-1.108\pm0.011}$ up to 21 ks, the X-rays show a strong decay with a slope of $t^{-5.95\pm0.20}$, inconsistent with synchrotron emission. The UVOIR light curves show a shallow maximum at the beginning, with different peak times for the different bands due to the peak emission of the BB component passing through the spectrum. The second component emerging at around 10 days post-burst is the contribution of the underlying SN, modeled with the GRB-SN 1998bw as a template, stretched in time by a factor of 1.25 and decreased in luminosity by a factor of 12 (see appendix for more details).

emission requires that the material observed cannot be directly connected to the stellar explosion itself but dense material has to have been ejected some time before the explosion.

An appealing possibility to explain GRB 101225A is a He-merger model with a common envelope (CE) phase

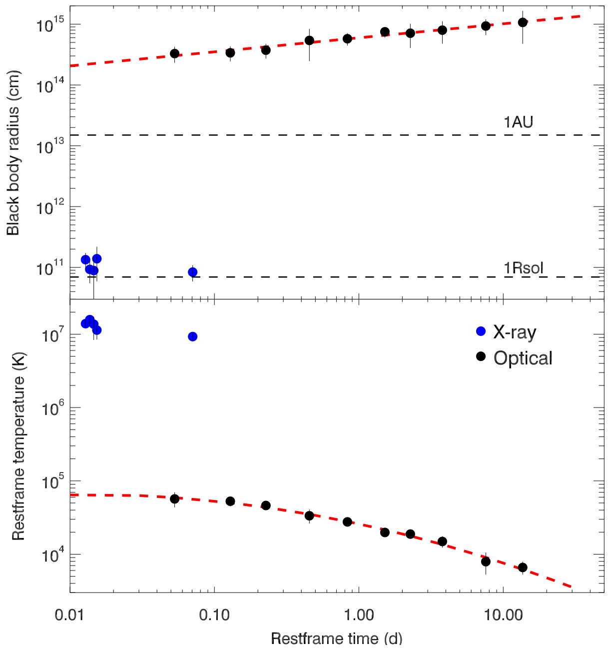

FIG. 3.— Evolution of the temperature and radius of the BB components in X-ray (blue dots) and UVOIR (black dots), excluding the data beyond 10 d when the SN component becomes dominant. The red dashed lines show the fit to the evolution of the UVOIR BB alone which shows that the optical BB emission is not simply from the cooling of the initial BB component in X-rays. The evolution of the radius of the UVOIR BB follows a power-law with R $\propto t^{0.23\pm0.02}$, incompatible with a Sedov-Taylor evolution as assumed for late-time SN evolution. The temperature decline does not follow a simple power-law which is well explained with a gas sphere cooling due to combination of expansion and radiation loss (see SI).

that has been proposed as a progenitor for GRBs (Fryer et al. 1998; Zhang et al. 2001; Barkov et al. 2010). In this model, a binary system consisting of two massive stars survives the collapse to a neutron star or black hole of the more massive component. When the second star moves off the main sequence and expands, it engulfs the compact remnant, leading to a CE phase and the ejection of the hydrogen and part of the helium core as the compact remnant spirals into the center of the second star Assuming the inspiral takes about 5 orbits or 1.5 yr and material is ejected at escape velocity, the outer ejecta are at a few 10^{14} cm when the compact remnant reaches the center of star, consistent with the radius of the outer BB we observe in the optical. Although angular momentum will preferentially eject material along the orbital plane, CE simulations suggest that the ejecta can form a broad torus which fits to our observations (see appendix). When the compact companion reaches the center of the second star, angular momentum forms a disk around the compact remnant, allowing the formation of a GRB-like jet. The remnant of this merger might be a magnetar whose prolonged activity is responsible for the very long duration of the actual GRB.

The jet and the subsequent breakout of the supernova can explain the power-law and thermal component in the X-rays of GRB 101225A. The shock-breakout X-rays irradiate the common envelope ejecta at a few times 10^{14} cm, where they get thermalized, explaining the UVOIR emission in the first 10 d of the explosion. As the supernova shock expands beyond the CE, it provides a final burst of emission, explaining the bump at $\sim$30 d in the light curve. The He-NS merger scenario naturally assumes a relatively small Ni-production, leading to a weak SN.

5. COMPARISON WITH OTHER EVENTS

A similar scenario might also explain XRF 060218 with a dense shell of material having been ejected prior to the main explosion, probably with a different progenitor system producing a brighter SN and a fainter GRB component (see appendix). On the other hand, a group of GRBs exists which feature an initial thermal component in X-rays (e.g., GRB 090618) due to the shock breakout, but which are accompanied by a classical, bright afterglow produced by the interaction of the jet with a moderately dense circumstellar medium (Cano et al. 2011). We therefore suggest that GRB 101225A was a member of a new class of "blackbody-dominated" long-duration GRBs connected to SNe which are arising in a very dense environment created by the massive-star progenitor or progenitor system itself, fully thermalizing the high-energy output from the collapsing star. The non-relativistic and isotropically distributed emission of such a component makes it difficult to detect such an event at higher redshifts making GRB 101225A a fortunate coincidence to derive conclusions about the progenitor system and its environment.

We thank J. S. Bloom for helping with the Keck observations and the staff of the various observatories for excellent support. The first author acknowledges a personal connection to the event 31 years prior to the burst. The Dark Cosmology Centre is funded by the DNRF. KLP acknowledges the support of the UK Space Agency. JG, AJCT, SG and PK are partially supported by the Spanish programs AYA-2007-63677, AYA-2008-03467/ESP, and AYA-2009-14000-C03-01. HTJ acknowledges support by DFG grants EXC153, SFB/TR27, and SFB/TR7. MAA is partly funded through grants AYA2007-67626-C03-01 and Prometeo-2009-103. PM acknowledges the support from MICINN through grants AYA2007-67626-C03-01 and CSD2007-00050. SRO and MDP thank STFC for financial support. MI, WKP, CC, JL, CJ, and SP acknowledge support from the CRI grant 2009-0063616, funded by the Korean government (MEST). AM acknowledges support from MK-405.2010.2.

APPENDIX

A. BAT DATA ANALYSIS AND FITTING

GRB 101225A was detected by BAT onboard the *Swift* satellite (Gehrels et al. 2004) on Dec. 25, 2010 at $T_0 =$ 18:37:45 UT as an image trigger (Racusin et al. 2010). It was already in progress both when the source entered the BAT field of view and when it left the field of view due to Swift orbit-constrained slews (Palmer et al. 2010; Cummings et al. 2010). Therefore, we can only give lower limits on the total burst fluence and the T_{90} duration. The total fluence of the intervals covered in the observations adds up to $(5.6 \pm 0.7)\times 10^{-6}$ erg cm^{-2} (implying a total energy release in γ-rays of $E_{\gamma,iso} > 1.4 \times 10^{51}$ erg), which is a lower limit to the total gamma-ray emission. No emission was detected in a previous observation of the field at $T - T_0 = -4950$ s. The lower limit on the duration is $T_{90} > 2000$ s. This is one of the highest durations ever observed for a *Swift* GRB, comparable to the longest burst observed by *Swift*, GRB 090417B (Holland et al. 2010). Fig. 4 shows the BAT light curve. The BAT-observed peak flux of $(3.25\pm0.47) \times 10^{-9}$ erg cm^{-2} s^{-1} in the $15-150$ keV range occurred in the interval $T - T_0 = +1372$ to $T - T_0 = +1672$ s. No other γ-ray instrument detected GRB 101225A, although the MAXI instrument on board the ISS ($2 - 10$ keV) reported a marginal detection at $T - T_0 = +1002$ s coincident with the BAT position (Serino et al. 2010).

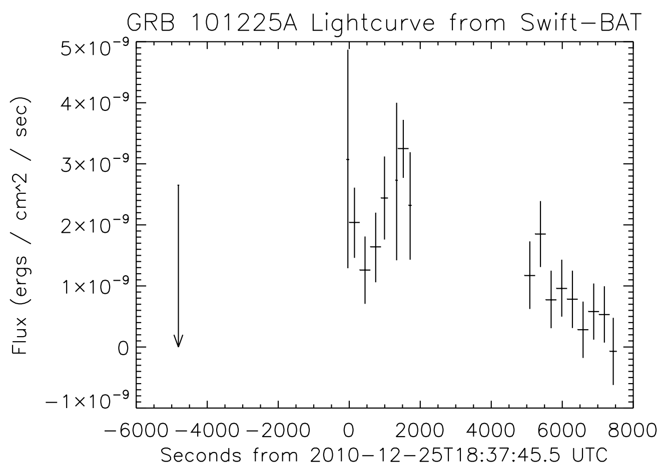

FIG. 4.— Flux in the $15-150$ keV band using a fixed power-law index of $\Gamma = 1.867$ from a fit to the most intense part of the burst. Note that the burst started before the beginning of the BAT data at $\sim T - T_0 = -100$ s and probably continued while the source was not in the BAT field of view from $T - T_0 = +1091$ to $T - T_0 = +1372$ s. The latest upper limit before the burst was 2.65×10^{-9} ergs cm^{-2} s^{-1} at $T - T_0 = -4950$ s. Error bars are at 90% confidence.

The time-averaged spectra from T_0 to $T - T_0 = +963$ s and from $T - T_0 = +1372$ to $T - T_0 = +1672$ s are best fit by simple power-law models with photon indices of $\Gamma = 1.91 \pm 0.35$ and 1.87 ± 0.21, respectively. For these fits the total fluences in each time period in the $15 - 150$ keV band are $(1.7 \pm 0.4)\times10^{-6}$ and $(9.0 \pm 0.2)\times10^{-7}$ erg cm^{-2}. All the quoted errors are at the 90% confidence level. The BAT spectra are almost equally well parametrised by models using a cutoff power-law or a blackbody to fit the data due to the low signal-to-noise ratio of the event. E_{peak} using a cutoff model is poorly constrained to 38 ± 20 keV. The blackbody temperature fit gives $kT = 10.1 \pm 1.1$ keV. Errors are at the 68% confidence level.

We also examined the BAT data to search for persistent emission after the trigger. For this we used the daily sky image mosaics produced as part of the BAT hard X-ray transient monitor which cover a single energy band of $15 - 50$ keV. We found a 5.3σ excess (0.0048 ± 0.0009 count cm^{-2} s^{-1}) on Dec. 25, 2010 (MJD 55555), the day of the trigger, and a positive excess in the count rate ($\geq 1\sigma$ or 0.0011 count cm^{-2} s^{-1}) over the next ten days (until MJD 55565). We determine the probability that such a sequence of excess rates would occur by chance. To do this, we examine the light curves of 106 "blank sky" points tracked in the BAT transient monitor. These are points chosen randomly across the sky at least 10 arcmin from any known X-ray source. Any positive flux from these points is expected to be due to chance fluctuations. In these 106 light curves ($> 200,000$ data points), we find only one sequence of six consecutive days showing a positive excess and none with more than six days. This means that the chance probability of ten days of excess flux is less than 1/200,000, so the observed prolonged emission is likely real.

B. XRT DATA ANALYSIS AND FITTING

The Swift-XRT data were processed with version 3.7 of the XRT data reduction software (released as part of `HEASoft 6.10` on 2010-09-28) and the corresponding calibration files used for subsequent spectral analysis. Data were collected in Windowed Timing (WT) mode for the first 7.3 ks after the trigger followed by Photon Counting (PC) mode for the rest of the observations. The object was detected by XRT from 1.4 ks to 10^5 s after the trigger. The peak flux in X-rays is 4.3×10^{-9} erg cm^{-2} s^{-1}, the total observed fluence 8.2×10^{-6} erg cm^{-2}, the unabsorbed fluence 1.1×10^{-5} erg cm^{-2}. At $z = 0.32$ this corresponds to a total energy release in X-rays of 3.6×10^{51} erg. Spectra were extracted for individual snapshots of data (one snapshot corresponds roughly to one orbit constrained by the observability of the object during the orbit) and were further timesliced into 100 s bins for the initial snapshot ($1.4 - 1.8$ ks after the trigger).

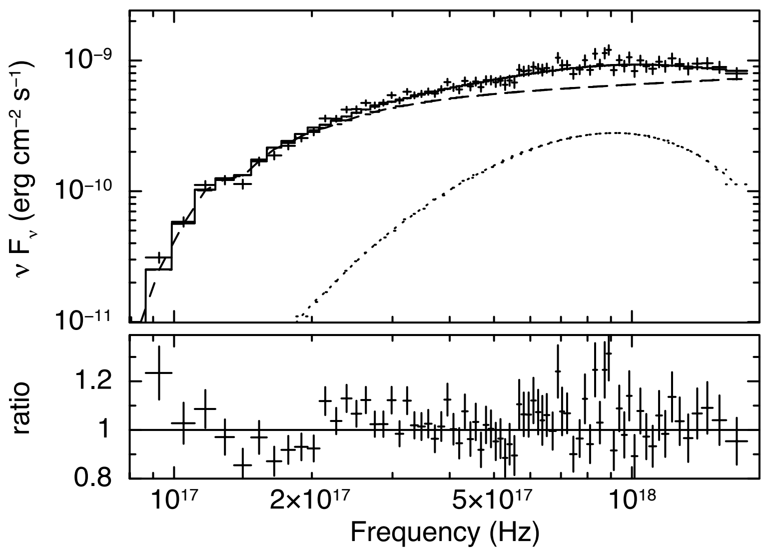

FIG. 5.— Fitting of the X-ray spectra from XRT in the first snapshot (top panel). The dashed line indicates the contribution of the power-law component, the dotted line shows the BB component. In the bottom panel we show the ratio between the observed data and the fitted model.

We tried a variety of fits to the X-ray data, using `XSPEC version 12.6.0`, with the result that an absorbed power-law plus blackbody component provided a good fit to the data (see Fig. 5). The Tübingen-Boulder absorption model was used, with the Wilms abundances (Wilms et al. 2000) and Verner absorption cross-section (Verner et al. 1996). As shown in Fig. 6, there is little spectral evolution within the first snapshot of data, with the best fit for the full 367 s of data being a power-law of photon index $\Gamma = 1.83^{+0.13}_{-0.10}$, a blackbody of temperature 0.96 ± 0.13 keV (1.11×10^7 K) and a total absorbing column of $(2.2 \pm 0.3)\times10^{21}$ cm^{-2}, for a χ^2 of 420.7 for 379 degrees of freedom. The Galactic column density in this direction is 7.9×10^{20} cm^{-2}. The inclusion of the BB is significant at the $> 99.9999\%$ level, the contribution of the BB to the total emission is around 20% (see Fig. 6). The second snapshot of data (also in WT mode) is again better fit with a BB in addition to the power-law, with $\Gamma = 2.18^{+0.12}_{-0.09}$, black-body kT $= 0.99^{+0.15}_{-0.17}$ keV and NH $= (2.7 \pm 0.2) \times 10^{21}$ cm^{-2}, with χ^2/dof $= 378/421$. This BB is significant at 99.987%. For the X-ray data after the second snapshot, no BB component is required and a simple absorbed power-law provides an acceptable fit, likely due to the lower signal at later times.

We also checked for possible periodicity in the X-ray data. To that end, light curves were extracted with 18 ms bins which is the best time resolution available for WT mode. Using the `Kronos powspec` tool, no significant periodic signal was identified with a frequency between 0.005 and 28 Hz (0.04 and 200 s) in either the first or second snapshot of data.

C. UV, OPTICAL AND IR DATA ANALYSIS

C.1. *Swift/UVOT*

Swift/UVOT began observing GRB 101225A 1373 s after the BAT trigger, simultaneous with the XRT observations. The automatic target sequence did not commence until the end of the BAT image trigger at ~ 23 minutes. The source was found to be blue, with strong detections in the UV filters (*uvw*1, *uvm*2, *uvw*2), weak detections in the *b* and *u*

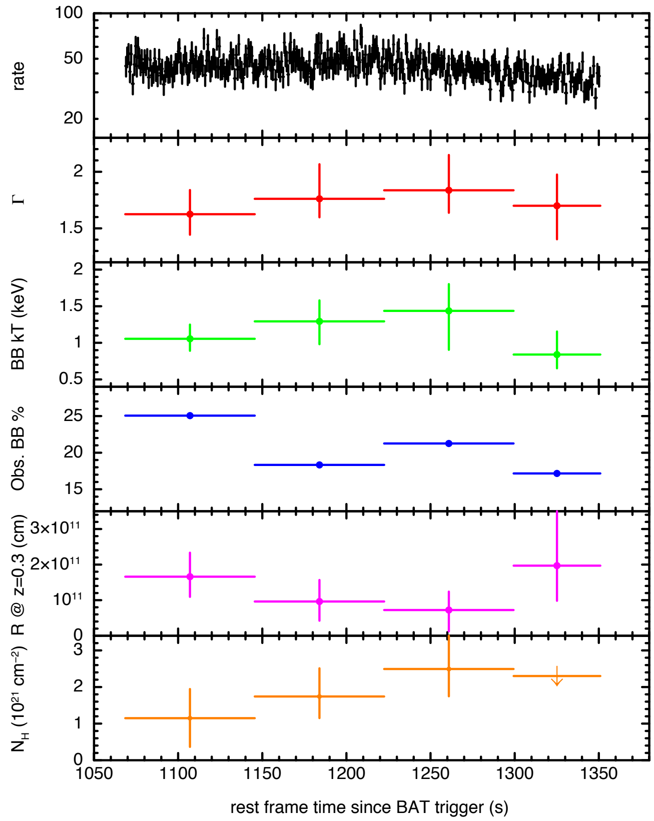

FIG. 6.— Results from the fits to the first snapshot of the X-ray data. The panels show from top to bottom: 1. The count rate during the first snapshot, 2. the photon index Γ, 3. the BB Temperature in keV, 4. the contribution of the BB to the total emission in percent, 5. the radius of the emitting BB at $z = 0.3$ and 6. total absorbing column density in X-rays (the Galactic column density in the line-of-sight is 7.9×10^{20} cm^{-2}).

filters, and no detection in the v filter. The data were processed using the standard *Swift* software tool `uvotmaghist` within `HEAsoft 6.9` and the latest calibration files (20101231).

We extracted counts using a circular aperture with a radius of 5 arcsec where the count rate was above 0.5 counts s^{-1}, and 3 arcsec aperture where the count rate had dropped below 0.5 counts s^{-1}, and a source-free background region. The tool `uvotmaghist` applies coincidence-loss corrections and aperture corrections. The count rates were converted to flux density using the standard photometric calibration (Poole et al. 2008; Breeveld et al. 2010).

C.2. *McD 2.1m*

The CQUEAN instrument (Camera for QUasars in the EArly uNiverse; Park et al. 2011, in preparation) on the 2.1m Otto-Struve telescope at McDonald Observatory, Texas, USA, observed the optical counterpart starting at 01:16:23 UT, on Dec. 26, 2010, or 6.64 h after the burst. Three exposures of 300 s were taken in r', i', z', and Y bands each under photometric conditions. The data were reduced with standard procedures of dark and flat-field corrections. The afterglow is detected in the r', i', and z'-band images, the Y band only give an upper limit.

C.3. *CAHA 1.23m*

The 1.23m telescope is located at the German-Spanish observatory of Calar Alto (CAHA) in Almería, Spain and is equipped with an optical imaging camera. The optical counterpart was detected in the VRI bands $1.04 - 1.11$ d after the GRB trigger. The 1.23m was also used to calibrate the object field in $BVRI$ bands by observing the Landolt fields RU149D and SA98 on Dec. 26 and 27, 2010 under photometric conditions.

C.4. *LT 2.0m*

The Liverpool telescope is a 2.0m fully robotic telescope located at the observatory of Roque de los Muchachos on La Palma. Observations were carried out with the imaging camera RATCAM. The optical counterpart was detected in a single i'-band epoch at in a single epoch at 10.09 d after the GRB.

C.5. *OSIRIS/GTC*

We acquired imaging data using OSIRIS at the Gran Telescopio de Canarias (GTC), a 10.4m telescope located at the observatory of Roque de los Muchachos on La Palma, Canary Islands, Spain.

The observations started in r' band $\sim$2 days after the burst, exposing for 30 s. A second r' observation was carried out $\sim$ 21 days after the gamma-ray event based on 5 exposures of 180 s. We furthermore obtained a late-time SED at 39 days in g', r', i' and z' bands and a last image at $\sim$44 days in the r' band.

The data of our two last epochs (at $\sim$39 and $\sim$44 days) were obtained at a considerable airmass (2.14>1.73) since the object was setting quickly after evening twilight. The data at $\sim$21 and $\sim$44 days were acquired with the proximity of the Moon at $\sim$54 and $\sim$36 degrees, when the illumination was 83% and 21%, respectively. The SED at 39 days was constructed in dark time. The observing conditions were good in our four GTC epochs.

C.6. *3.6. Gemini-North: NIRI and GMOS-N*

Late-time imaging of the optical counterpart of GRB 101225A was conducted with the Gemini-North observatory on Mauna Kea/Big Island, Hawaii, on several occasions. On the night of Jan. 23, 2011 we observed the field with the Near InfraRed Imager (NIRI) in the K' filter for 44×60 s exposures (2×30 s co-adds) before switching to the Gemini Multi-Object Spectrograph (GMOS-N) for 5×180 s exposures each in the r' filter. On the night of Feb. 01, 2011 we re-observed the field with NIRI in the J band for 32×60 s exposures (1 co-add), and finally on the night of Feb. 03, 2011 we imaged the field in all four GMOS broad-band filters ($g'r'i'z'$). Since the source was setting, all exposures were taken at moderate to high airmass ($1.5 - 2.5$), although under relatively good seeing conditions.

C.7. *BTA 6m*

A final late image was obtained using SCORPIO on the 6.0m BTA telescope, located at the Special Astrophysical Observatory, in Russia. The observation consisted of 20×120 s exposures using an I filter obtained on Feb. 25, 2011 under good weather conditions and a seeing of $1.3 - 2.0$ arcsec.

C.8. *Photometry of ground-based data*

The photometry of V, R and I data was done in a consistent way using a set of 15 comparison stars in the field of GRB 101225A calibrated with the Landolt fields taken on Dec. 26 and 27, 2011 by the 1.23m CAHA. For r', i' and z', photometric calibration was done with observations of the 2.1m Otto-Struve telescope at McDonald Observatory on Dec. 26, 2010, using standard star data (Feige 34). Finally, g' photometry was derived from the rest of the reference magnitudes using numerical transformations (Jester et al. 2005). The magnitudes of the comparison stars in the different filters used for the optical observations are listed in Tab. 1.

We performed aperture photometry using PHOT within IRAF assuming an aperture radius equal to the Full Width at Half Maximum (FWHM) of the stellar point sources. In a few cases, where the contamination by neighboring sources was not negligible, PSF photometry within IRAF was carried out. In Tab. **??** we list the final photometry for all UV, optical and IR data.

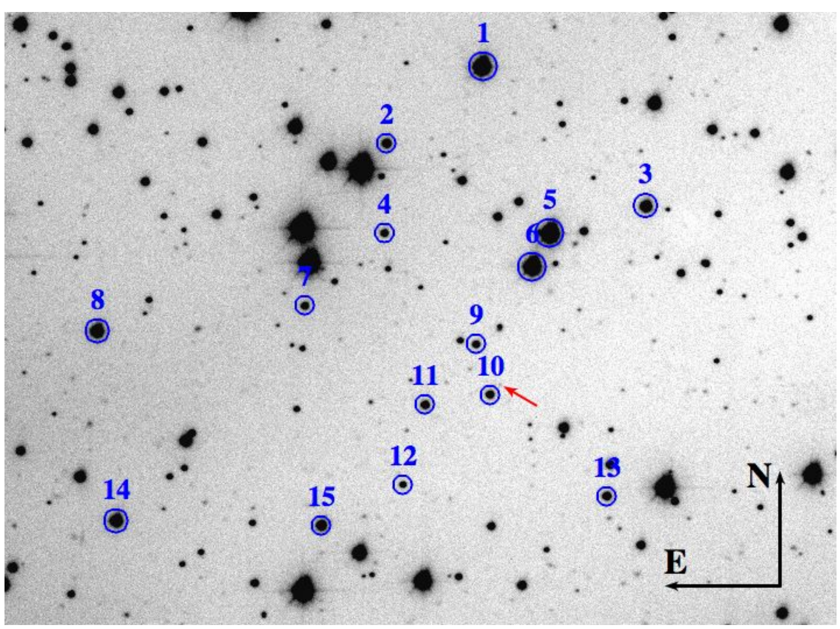

Fig. 7.— Secondary standards used for the photometric calibration. The position of the optical counterpart of GRB 101225A is indicated with a red arrow. The photometric magnitudes of each of the reference stars are given in Table 1. The field of view is $6' \times 4'$.

TABLE 1
MAGNITUDES OF CALIBRATION STARS USED FOR THE OPTICAL PHOTOMETRY. A FINDING CHART INDICATING THE POSITION OF EACH REFERENCE STAR IS GIVEN IN FIG. 7. V, R AND I ARE GIVEN IN VEGA SYSTEM, WHILE THE REST ARE IN AB.

ID	R.A. (J2000)	Dec. (J2000)	V	R	I	g'	r'	i'	z'
1	00:00:48.13	+44:38:18.9	15.282 ± 0.009	14.916 ± 0.049	14.553 ± 0.052	——	——	——	——
2	00:00:52.02	+44:37:46.6	18.065 ± 0.097	17.268 ± 0.055	16.288 ± 0.110	18.62±0.23	17.679±0.011	17.121±0.010	16.870±0.010
3	00:00:41.58	+44:37:18.0	16.794 ± 0.050	16.421 ± 0.051	15.972 ± 0.062	17.14±0.12	——	——	——
4	00:00:52.13	+44:37:07.9	18.789 ± 0.079	18.335 ± 0.133	18.051 ± 0.162	19.26±0.19	18.464±0.012	18.325±0.011	18.263±0.013
5	00:00:45.46	+44:37:06.6	14.995 ± 0.008	14.633 ± 0.049	14.235 ± 0.051	——	——	——	——
6	00:00:46.18	+44:36:52.4	15.174 ± 0.015	14.838 ± 0.049	14.456 ± 0.051	——	——	——	——
7	00:00:55.37	+44:36:36.8	19.165 ± 0.180	18.268 ± 0.090	17.356 ± 0.188	——	18.569±0.012	17.905±0.011	17.597±0.011
8	00:01:03.76	+44:36:26.8	16.594 ± 0.012	16.161 ± 0.049	15.691 ± 0.090	——	——	——	——
9	00:00:48.48	+44:36:19.3	18.796 ± 0.059	17.924 ± 0.069	16.694 ± 0.092	19.08±0.14	18.602±0.012	17.819±0.011	17.516±0.011
10	00:00:47.98	+44:35:57.8	18.682 ± 0.132	17.901 ± 0.107	17.059 ± 0.182	19.41±0.31	18.174±0.011	17.645±0.010	17.427±0.012
11	00:00:50.58	+44:35:43.5	18.505 ± 0.218	17.877 ± 0.060	17.270 ± 0.163	——	18.088±0.011	17.715±0.010	17.537±0.012
12	00:00:51.59	+44:35:19.1	19.253 ± 0.130	18.893 ± 0.131	18.460 ± 0.273	19.54±0.31	19.059±0.014	18.910±0.013	18.852±0.020
13	00:00:43.29	+44:35:13.1	18.050 ± 0.066	17.749 ± 0.085	17.318 ± 0.108	18.34±0.16	17.853±0.011	17.729±0.010	17.671±0.012
14	00:01:03.09	+44:35:04.8	16.828 ± 0.015	16.321 ± 0.052	15.826 ± 0.087	——	——	——	——
15	00:00:54.83	+44:35:01.9	17.516 ± 0.032	17.024 ± 0.066	16.321 ± 0.082	18.04±0.08	17.148±0.010	16.960±0.010	16.853±0.011

C.9. *Preimaging*

Preimaging of the field was obtained from the archive of the 3.5m Canada-France-Hawaii Telescope (CFHT). Observations were obtained with the MegaPrime/MegaCam for the Pan-Andromeda Archaeological Survey (PAndAS, Richardson et al. 2011). We combined 3×500 s exposures obtained under very good conditions in g' and i' bands. We derive 3σ limiting magnitudes for these exposures of $i' > 25.5$ and $g' > 26.9$. However, at the position of GRB 101225A, we detect a low-significance object in the g' band, for which we measure $r' = 27.2 \pm 0.5$, which could be the host galaxy of our source (see Fig. 8).

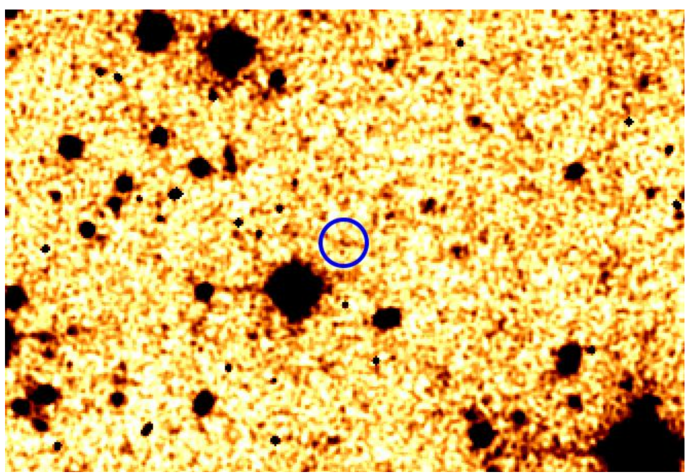

FIG. 8.— Pre-imaging exposure in g' band obtained with the 3.5m CFHT. The field of view is $60'' \times 40''$, North is to the top and East to the left of the image. The blue circle indicates the position of the optical counterpart of GRB 101225A, where we see a low significance detection of what could be the host galaxy.

D. OPTICAL SPECTROSCOPY

We obtained a spectrum of the optical counterpart 51 h after the event using OSIRIS on the 10.4m GTC telescope on La Palma (Spain). Two spectra of 1800 s exposure time each were taken with grism 300B (R=325, wavelength range: $3500 - 7000$ Å) under moderate to high airmass (1.26 and 2.05, respectively). The spectra were reduced and combined with standard tasks in IRAF and flux-calibrated with the spectrophotometric standard G191-2B2 taken the same night. The continuum is clearly detected, but the spectrum shows no obvious absorption or emission lines. The limits on the detection of Hα [OIII] and [OII] emission from the host galaxy are $< 5\times10^{-18}$ erg cm^{-2} s^{-1}, $< 2.3\times10^{-18}$ erg cm^{-2} s^{-1} and $< 3\times10^{-18}$ erg cm^{-2} s^{-1} (3σ) respectively. We can also put a limit on the detection of Hα at z=0 of $< 2\times10^{-18}$ erg cm^{-2} s^{-1}. The flux-calibrated spectrum with the position of typical emission lines from the host shifted to a redshift of $z = 0.32$ is show in Fig. 9.

On the night of 2011 Feb. 04 we observed the optical counterpart with the Low-Resolution Imaging Spectrometer (Oke et al. 1995) on the Keck I telescope during local twilight. Two undithered observations of 600 seconds each were acquired using the 1.0 arcsec slit and the D500 dichroic at a position angle of 86.5 degrees. On the red arm we

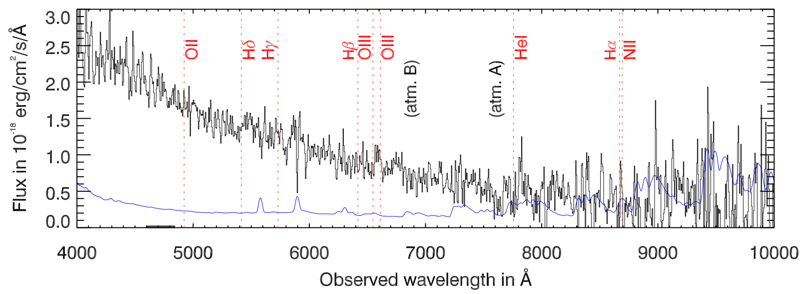

FIG. 9.— Flux-calibrated spectrum obtained with the GTC 2.1 days after the GRB. The error spectrum is plotted in blue. The red lines indicate the position of normally strong emission lines from the interstellar medium at a redshift of $z = 0.32$, none of the lines are detected in our spectrum.

used the 600/7500 grating and binned the CCD along the spatial direction (2x1 binning); on the blue arm we used the 600/4000 grism and binned the data along both spatial and spectral axes (2x2 binning). Due to twilight there is no evidence of a trace in the blue spectrum (and no source is detected in GMOS g'-band imaging from the previous night). A faint continuum trace at the expected position of the transient is identified on the red side in the second (less twilight-affected) exposure from 7160 to 8000 Å with no absorption or emission features visible.

E. MODELING THE UV TO NIR SPECTRAL-ENERGY DISTRIBUTION

Already the early evolution of the UV/optical/IR (UVOIR) counterpart proved to be very unusual for a GRB afterglow. Instead of a power-law spectrum with a negative spectral slope, it had a very blue counterpart, following what seemed to be a power-law with a positive spectral slope (Cenko et al. 2010). Furthermore, the counterpart stayed bright during the first days and then a decayed (Xu et al. 2010a) with a strong color change, transforming into a very red counterpart two weeks after the trigger (Tanvir et al. 2011). We interpret this early evolution as being produced by the expansion and cooling of a blackbody (BB), as shown in Section E.1.

The simple BB evolution is not valid any more for the emission beyong ~ 20 days after the trigger. At that time we observe a flattening of the light curve, while the very red color is preserved. This late evolution can be well-described with the presence of a supernova component, as described in Section E.2.

E.1. *Early time evolution*

For the modeling of the UVOIR spectral energy distribution (SED), we use the photometry presented here together with some of the data points extracted from the literature (Xu et al. 2010a,b; Wiersema et al. 2010; Cenko et al. 2010; Xu et al. 2011; Fynbo et al. 2011; Tanvir et al. 2011), all of which we correct of a Galactic extinction of $A_V = 0.33$ mag and transform from magnitudes to flux densities. The data allow us to derive a set of 12 SEDs ranging from 0.07 to 40 days after the trigger.

The early optical SEDs are well fitted by using an expanding and cooling blackbody of the following form (in frequency space):

$$F_\nu(Jy) = 10^{26}\left(\frac{R}{D}\right)^2 \frac{2\pi\nu^3(1+z)}{c^2}\frac{1}{e^{h\nu/k_B T_{obs}}-1} \tag{E1}$$

Here 10^{26} is used to convert $W/m^2/Hz$ to Jy. R is the radius of the emitting black body (which we assume to be spherical), D is the luminosity distance to the object, z the redshift and T_{obs} is the observed blackbody temperature (the rest-frame temperature would be $T_{rest} = T_{obs}(1+z)$). The others physical constants: c is the speed of light, h Planck's constant and k_B Boltzmann's constant. For simplicity we assume a blackbody with an emissivity of 1.

The blackbody succeeds in reproducing the data up to 10 days, without any intrinsic extinction or additional emission component, after which another component becomes dominant. We find that this second component can be reproduced with the spectral templates of SN 1998bw placed at a redshift of $z = 0.32^{+0.06}_{-0.07}$ with a stretching factor of 1.25 and a luminosity of 0.1 of SN 1998bw (see Section E.2).

From the fits to the SED evolution and allowing a second-degree fit, we get the following evolution of the normalisation-constant:

$$log\left(10^{26}\pi(1+z)\left(\frac{R}{D}\right)^2\right) = (0.70\pm0.04) + (0.46\pm0.03)log(t) - (0.01\pm0.05)log10(t)^2 \tag{E2}$$

where t is the time in days. The temperature evolution (in K) can be described by:

$$log\,(T_{obs}) = (4.342\pm0.017) - (0.395\pm0.016)log(t) - (0.11\pm0.02)log(t)^2 \tag{E3}$$

Figures 10 and 11 show the temporal evolution of the normalisation constant and the temperature. The normalisation can be sufficiently described by a linear evolution in log-log space and therefore the second order term in eq. (2) can be neglected. For the temperature, we need an additional second order term to obtain an reasonable fit to the data.

TABLE 2
MEASURED VALUES FOR THE BLACKBODY EVOLUTION. VALUES IN BRACKETS ARE NOT BE FITTED DUE TO A LIMITED AMOUNT OF DATA POINTS IN THOSE SEDS.

Epoch (days)	Observed temperature (K)	Normalisation constant $(1+z)\pi 10^{26}\left(\frac{R}{D}\right)^2$
0.07	(43 000±8 000	1.7±1.5)
0.17	40 000±6 000	1.8±1.2
0.3	35 000±3 950	2.2±0.8
0.6	25 340±5 440	4.6±2.5
1.1	20 900±1 770	5.2±1.2
2.0	15 000±1 090	8.9±1.8
3.0	14 260±1 760	8.00±3.4
5.0	(11 300±2 000	10.0±4.0)
10.0	(6 000±2 000	14.0±4.0)
18.0	(5 000±1 000	18.0±10.0)

The temperature evolution fits very well to a theroretical model of an expanding and homogeneously radiating gas sphere (see Fig. 20. Once the redshift is known the normalisation constant can be transformed into physical values in the rest-frame of the object which is shown in the Fig. 3 in the main paper. For this we assume $z = 0.32$ (see Section E.2), or 1661.1 Mpc using a ΛCDM cosmology with $H_0 = 71$, $\Omega_M = 0.27$ and $\Omega_\Lambda = 0.73$.

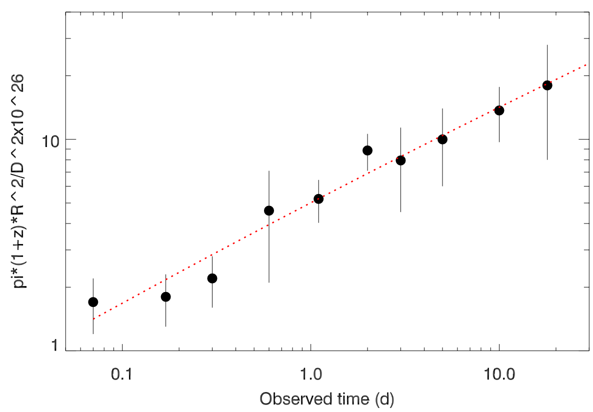

FIG. 10.— Evolution of the normalization constant.

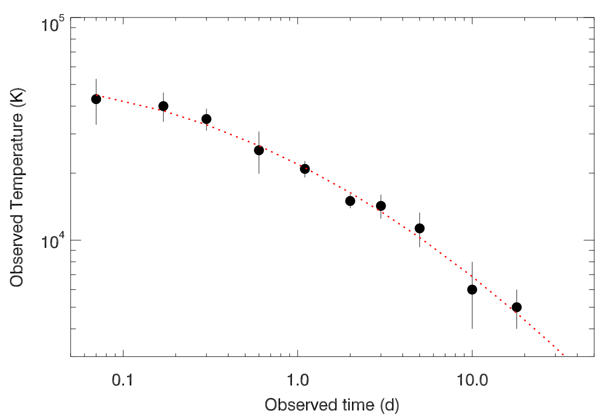

FIG. 11.— Evolution of the observed temperature requiring a second order term.

E.2. *Late evolution and SN template fitting*

The late evolution of the light curve requires a component in addition to the evolving BB described in Section E.1 which is best described by a combination of a supernova (SN) and a BB. In the following, we present the late SED

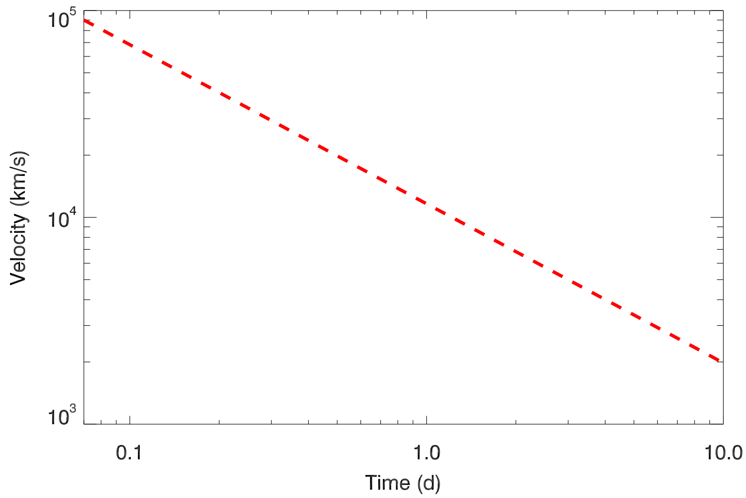

FIG. 12.— Evolution of the velocity of the black body according to the result of our modeling in the UVOIR range. During our observing period velocities of the range $0.3 - 0.07c$ are measured, typical of accelerated material during a supernova explosion.

fitting using several SN templates. We then take these fits to estimate the redshift of GRB 101225A, which we could not obtain spectroscopically (Section D).

To determine the redshift of GRB 101225A we use the SED at 40 days after the burst where the contamination from the BB is negligible and where we have 5 detections in different bands. Given the steep slope in the blue part of the spectrum, we convolve the response of each filter with the spectral shape of the templates. This is particularly important for the r'-band observations performed from GTC and Gemini at a very similar epoch, which show a significant difference in flux density. The filter of GTC reaches slightly redder wavelengths, and the difference in flux densities can be well explained by a very steep slope due to a SN feature as shown in Fig. 13.

We obtain templates for different core-collapse supernovae from the literature [25]. We exclude SN Ia from the analysis, as we do not expect a high-energy emission or BB evolution for those events. The template for each SN prototype was interpolated to the time of the SED for a range of redshifts (see references in Table 3). In the particular case of SN 1988S the templates were created by combining ground-based and HST spectra. For each SN template we evaluate the best fit for a range of redshifts, allowing a scaling of the flux of the supernova. Table 3 displays the results of the fits.

TABLE 3
FITS OF THE SED WITH SN TEMPLATES

SN Type	SN template	best fit z	$\chi^2/d.o.f.$	Reference
Ibc	1999ex	$0.24^{+0.06}_{-0.07}$	1.21	(Stritzinger et al. 2002)
Ic	1994I	$0.24^{+0.10}_{(-0.07)}$	1.21	(Richmond et al. 1996)
Ic broad-lined	1998bw	$0.32^{+0.06}_{-0.07}$	0.72	(Kulkarni et al. 1998)
II	1998S	$0.50^{+0.07}_{-0.08}$	8.90	(Anupama et al. 2001; Lentz et al. 2001; Fassia et al. 2001)
IIL	1985P	$0.40^{+0.06}_{-0.03}$	1.31	(Gaskell et al. 1992)
IIP	1999em	$0.40^{+0.05}_{-0.03}$	1.26	(Leonard et al. 2002)

The absolute best fit is obtained with a SN 1998bw template, a broad-lined Type Ic that is the classical reference for GRB-related supernovae. For this case we obtain a redshift of $z = 0.32^{+0.06}_{-0.07}$. The other core-collapse SNe we tested (excluding the Type II SN 1998S, which clearly does not fit our SED) give redshifts between $z = 0.24$ and $z = 0.40$, with an average value of $z = 0.32$, confirming our result using SN 1998bw. We therfore use z=0.32 as reference in this work. Figure 13 shows the fitted SED with the template at $z = 0.32^{+0.06}_{-0.07}$.

E.3. *Luminosity and stretching factor of the SN associated with GRB 101225A in context of other GRB-SNe*

We can undertake a more general comparison to SNe associated with GRBs by following the formalism of (Zeh et al. 2004). These authors used a SN 1998bw template light curve to fit late bumps in GRB afterglow light curves, modifying the template by increasing or decreasing the luminosity at peak (the parameter k, with $k = 1$ implying a peak luminosity identical to that of SN 1998bw), and stretching or compressing the light curve in time while retaining the overall shape (the parameter s, again, $s = 1$ implies the temporal evolution is identical to that of SN 1998bw in the same band). This procedure also included the creation of synthetic templates by interpolating between the SN

[25] http://supernova.lbl.gov/~nugent/nugent_templates.html

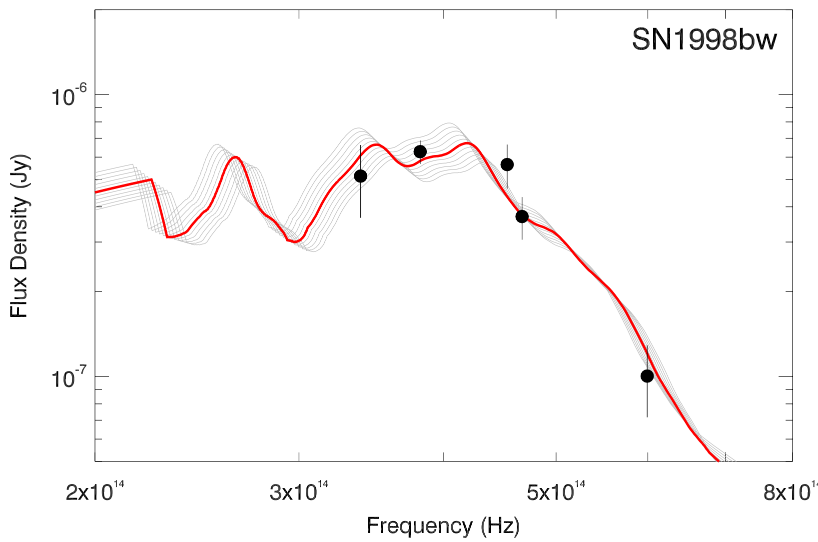

FIG. 13.— Fit of the day 40 SED to a SN 1998bw template. The observations are in black and the best fit, with a redshift of $z = 0.32$, in red. The gray lines represent the template at the different redshifts (steps of 0.01) within errors.

1998bw light curve in different filters, and taking into account the cosmological K-correction. Nearly all GRB-SNe were well-fit by the SN 1998bw light curve template. Using a supernova light-curve template of SN 1998bw redshifted to $z = 0.32$ to fit the late light curve of the GRB 101225A we find $s = 1.25 \pm 0.15$ and $k = 0.08 \pm 0.03$ using the designation of (Zeh et al. 2004).

Ferrero et al. (Ferrero et al. 2006) analyzed SN 2006aj associated with XRF 060218, and placed it into the $k - s$ context. They employed the line-of-sight extinction values derived by (Kann et al. 2006) to derive intrinsic k values. To place the SN associated with GRB 101225A into the $k - s$ context, we fit the light curve analogous to (Zeh et al. 2004), and use the sample of (Ferrero et al. 2006) as well as additional events as a comparison. The complete data is presented in Table 4.

GRB 990712 has been analysed again with additional data. We find no evidence for host extinction. For GRB 021211, a re-analysis of the afterglow SED finds no evidence for host extinction, the value from (Ferrero et al. 2006) thus remains unchanged but now counts as extinction-corrected. For GRB 040924, we use the k and s values from (Wiersema et al. 2008) and correct k with the extinction found by (Kann et al. 2006). For GRB 050525A, we use the uncorrected k value from (Ferrero et al. 2006), and correct it with the extinction found by (Kann et al. 2010). For XRF 050824, we use the uncorrected k value from (Sollerman et al. 2007), and correct it with the extinction found by (Kann et al. 2010). GRB 060729 is analysed in (Kann et al. 2011). GRB 080319B is analysed in (Bloom et al. 2009). GRB 090618 has been analysed for this work, using the data set of (Cano et al. 2011). We were not able to derive a good SED for this afterglow, therefore the k value has not been corrected.

As can be seen in Fig. 14, the SN associated with GRB 101225A is significantly fainter than any other known GRB SN (with the SN associated with GRB 040924 being the most similar, but this event is only marginally detected). At the same time it is similar in temporal evolution, actually being slower than most known GRB-SNe, though not by a large amount. It is also fainter than two well-studied Type Ic SNe, SN 1994I and SN 2002ap (see (Ferrero et al. 2006) for discussion), the latter being broad-lined, but not associated with a GRB.

F. REDSHIFT DETERMINATION

Determining the distance scale at which GRB 101225A occurred is crucial to understand the energetics and get a clear picture of the physics involved in this event. The following independent argument are used to strengthen our redshift estimation. The first strong limit on the redshift comes from the UVOT detection in $uvw2$ which implies a redshift lower than $z = 1.4$ (Campana et al. 2010).

From the SED fit of the first days, we know that the evolution is well-described by a simple BB. Depending on the distance at which the object is found, we can derive different radii and expansion velocities. For an explosion of this type, we expect expansion velocities larger than $\sim 10^3$ km s^{-1}, which would be barely equivalent to a stellar wind and, if similar to a SN explosion, of the order of 10^4 km s^{-1}. We cannot, in principle, rule out higher velocities in the ejecta. However, higher velocities would have further implications. As the velocity of the ejecta is accelerated to velocities close to c, we would expect to see a broadening in the shape of the blackbody SED due to the fact that the equal-arrival-time surface would be covering regions of different temperatures.

Making the assumption that the ejecta should not be traveling at velocities larger than 150,000 km s^{-1} ($0.5c$) and lower than 1,000 km s^{-1} ($0.03c$), we can estimate an acceptable redshift range between $z = 0.20$ and $z = 0.60$. At a redshift of $z = 0.32$, the velocity of the blackbody would have evolved from $\sim 90,000$ km s^{-1} at the time of our

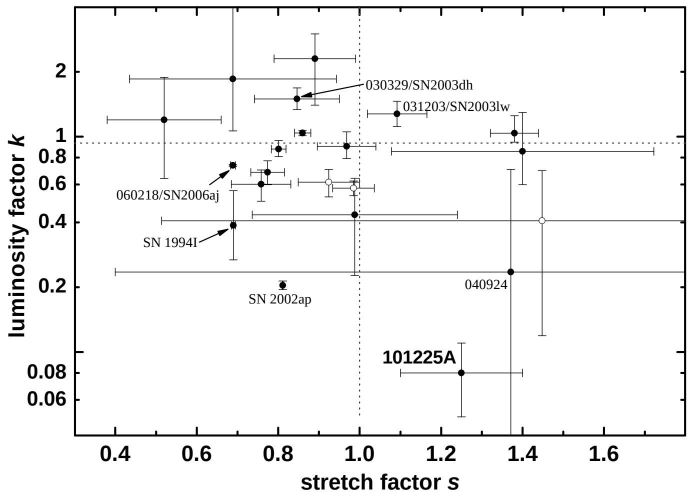

FIG. 14.— Luminosity factor k and stretch factor s of SNe associated with GRBs. Filled symbols have been corrected for host-galaxy line-of-sight correction, non-filled symbols have not. We label several well-studied nearby GRB-SNe. We label several well-studied nearby GRB-SNe, as well as two "canonical" Type Ic SNe, SN 1994I (Ic) and SN 2002ap (broad-lines Ic unassociated with a GRB). The GRB 101225A SN is fainter than all these events.

TABLE 4
LUMINOSITY FACTOR k AND STRETCH FACTOR s FOR GRB SNE

GRB	k	s	Comment	Source
970228	0.41 ± 0.29	1.45 ± 0.93	uncorrected	Ferrero et al. (2006)
990712	0.60 ± 0.10	0.76 ± 0.07		This Work
000911	$0.85^{+0.44}_{-0.26}$	1.40 ± 0.32		Ferrero et al. (2006)
010921	$1.85^{+2.82}_{-0.79}$	0.69 ± 0.25		Ferrero et al. (2006)
011121	$0.88^{+0.08}_{-0.07}$	0.80 ± 0.02		Ferrero et al. (2006)
020405	$0.90^{+0.15}_{-0.11}$	0.97 ± 0.07		Ferrero et al. (2006)
020903	0.62 ± 0.09	0.92 ± 0.08	uncorrected	Ferrero et al. (2006)
021211	0.43 ± 0.21	0.99 ± 0.25		Ferrero et al. (2006), This Work
030329	$1.50^{+0.19}_{-0.16}$	0.85 ± 0.10		Ferrero et al. (2006)
031203	$1.28^{+0.18}_{-0.16}$	1.09 ± 0.07		Ferrero et al. (2006)
040924	$0.24^{+0.47}_{-0.23}$	1.37 ± 0.97		Wiersema et al. (2008), Kann et al. (2006)
041006	$1.04^{+0.22}_{-0.09}$	1.38 ± 0.06		Ferrero et al. (2006)
050525A	$0.68^{+0.09}_{-0.08}$	0.77 ± 0.04		Ferrero et al. (2006), Kann et al. (2010)
050824	$1.20^{+0.69}_{-0.56}$	0.52 ± 0.14		Sollerman et al. (2007), Kann et al. (2010)
060218	0.74 ± 0.01	0.69 ± 0.01		Ferrero et al. (2006)
060729	1.04 ± 0.03	0.86 ± 0.02		Kann et al. (2011)
080319B	$2.30^{+0.70}_{-0.90}$	0.89 ± 0.10		Bloom et al. (2009)
090618	0.58 ± 0.05	0.99 ± 0.05	uncorrected	This Work, Cano et al. (2011)
101225A	0.08 ± 0.03	1.25 ± 0.15		This Work

first SED to $\sim 2,000$ km s^{-1} at the time of our last blackbody-dominated epoch, nicely matching the requirements. The fact that the blackbody detected for XRF 060218/SN 2006aj was very similar to the one found for GRB 101225A when placed at a redshift of $z = 0.32$ (see Section G) adds additional evidence for the validity of the redshift estimate.

In conclusion, the assumption that GRB 101225A is located at a redshift of $z = 0.32^{+0.06}_{-0.07}$ is supported by independent factors, and can be considered as a firm reference when studying the physical processes involved in the event. In any case we do not expect redshifts significantly smaller than $z = 0.2$ or higher than $z = 0.4$.

G. COMPARISON BETWEEN GRB 101225A AND OTHER GRBS WITH SNE AND BB COMPONENTS

In Table 5, we compare some properties of GRBs which were associated to SNe and did not show a "classical" afterglow component. All of them are subluminous compared to the average long-duration GRB with E_{iso} around 10^{51}–10^{54} erg. GRB 101225A, however, lies on the lower end of normal long-duration GRBs. Among those nearby GRB-SNe without a classical afterglow, there seems to be a class of very long duration GRBs with very low E_{peak} values, all of them showing a thermal component in X-rays. GRB 060218 and XRO 080109 also had a thermal component at optical wavelengths during the first few days (Campana et al. 2006; Soderberg et al. 2008). For 100316D, no optical counterpart was detected before the onset of the actual SN due to high intrinsic extinction in the host galaxy.

XRF 060218 (Campana et al. 2006) shows a similar early behavior to GRB 101225A. We compare the early UVOT lightcurve of XRF 060218, which we obtained from the UVOT catalogue (Roming et al. 2009), to the lightcurve from GRB 101225A by shifting the XRF 060218 to z=0.3 including a k-correction. To obtain the k-correction, we use

TABLE 5
GRBs with SNe but without afterglows

GRB	z	TC?	T_{90}	E_{peak} (s)	E_{iso} (erg)	HR(50-100) (erg)	Radio?	SN M_V (mag)	Host M_B (mag)
980425	0.0085	No	23.3	55±21	8.1×10^{47}	...	Yes	-19.42	-17.6
031203	0.105	No	30	158±51	3×10^{49}	...	Yes	-20.39	-21.0
060218	0.0331	Yes	∼2100	4.9	6.2×10^{49}	0.835	Yes	-18.76	-15.9
080109*	0.0065	Yes	∼400	low	2×10^{46}	...	Yes	-16.7	-20.7
100316D	0.059	Yes	>1300	...	3.1×10^{49}	0.891	No	...	-18.8
101225A	0.32	Yes	>1600	38±20	$> 1.4\times10^{51}$	1.06	No	-16.9	> -14.0

*No γ-rays observed, numbers derived from X-rays.
TC? refers to the early thermal component, mostly attributed to a supernova breakout.
HR is the hardness ratio, defined as the ratio of channels $(50-100\ \mathrm{kev})/(25-50\ \mathrm{keV})$
SN M_V is the SN peak absolute magnitude in V
Host M_B is the host absolute magnitude in B

a
b
c
d
e

`XSPEC` assuming a blackbody spectrum with kT ~ 3.7 eV. The temperature was determined from the best-fit model of a BB to a SED of XRF 060218 taken at 120 ks after the trigger (Campana et al. 2006). Using this BB spectrum, we determined the expected flux density in the observed frame for each filter and at $z = 0.32$. The ratio of these two flux densities was taken to be the k-correction for the specific filter, which is ~ 2.20 for all filters. Figure 15 compares the flux density light curves of the 3 UV filters of both GRBs. For both GRBs the light curves were corrected for Galactic extinction.

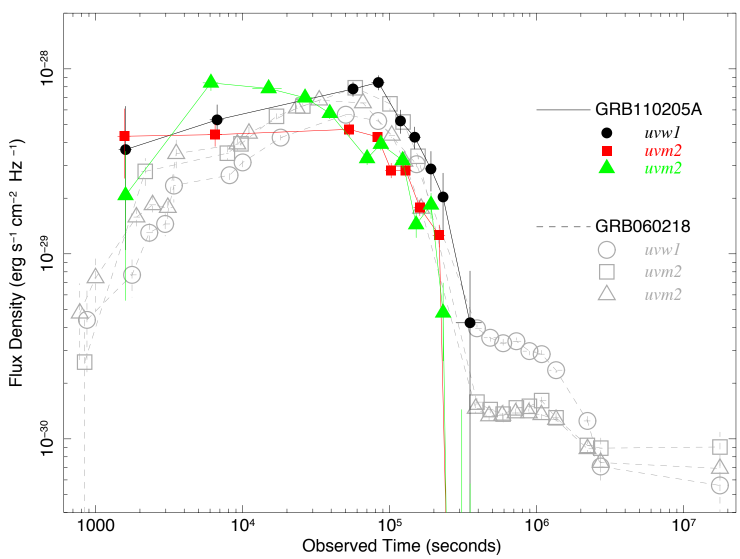

Fig. 15.— The 3 UV fliter light curves in flux density for GRB 101225A and XRF 060218. The light curves for XRF 060218 have been shifted to z=0.3 for direct comparison. The colored solid shapes connected by solid lines are for GRB 101225A, open symbols and dotted lines for XRF 060218. Circles are $uvw1$, squares are for $uvm2$, triangles are $uvw2$.

To complete this, we performed a fit of the early UVOIR SEDs of XRF 060218 and XRO 080109, in a similar way to what we did for GRB 101225A. XRF 060218 also seems to follow a black body evolution at early times. However, the SN starts to dominate already around 3 days after the burst, limiting the possible study of the evolution. As it can be seen from Fig. 16 and 17, the evolution of the black body is not very different from what we see in GRB 101225A although the radius expansion is slightly steeper. XRO 080109 does not have a measurable thermal component in the early X-ray data. In the optical, the cooling BB dominates until about 4 days after the event when the onset of the SN was observed (for the SED fitting see Fig 18). The temperature of the UVOIR BB of XRO 080109 is lower (~ 30 000 K) than those of XRF 060218 and GRB 101225A. The radius evolution is considerably steeper than for those two events (Fig 19). The UVOIR BB emission of XRO 080109 is therefore likely due to the cooling of the initial shock breakout.

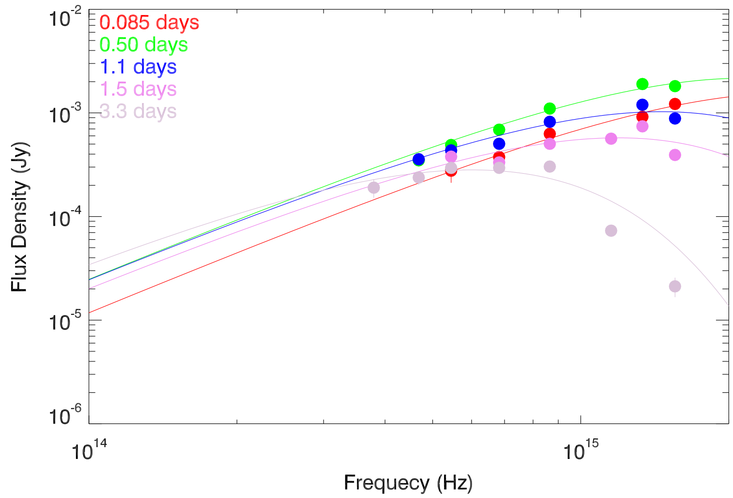

FIG. 16.— SED fit of the early UVOIR data of XRF 060218/SN 2006aj. The last epoch already begins to show a strong contribution of the SN.

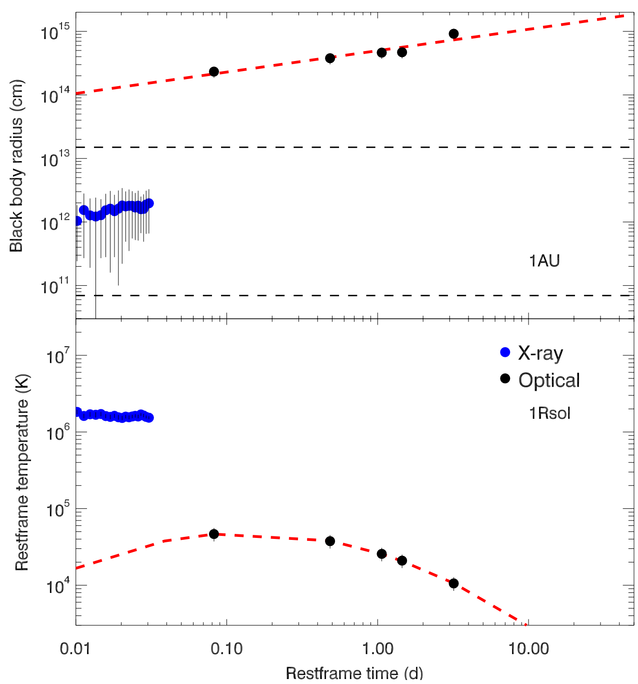

FIG. 17.— Temporal evolution of the radius and temperature for the pre-SN epochs of XRF 060218/SN 2006aj. This figure can be directly compared with Fig. 3 of the main text.

H. TEMPERATURE EVOLUTION AND GEOMETRY OF THE UVOIR BB

The temperature evolution of the UVOIR BB can be modeled with a hot, thick shell that was initially heated, e.g. by absorbed photons from the thermal and non-thermal sources of high-energy radiation, and then expands and cools by emitting photon energy. Approximating the radially extended shell (with the outer radius being much larger than the inner radius) as a homogeneous sphere, we apply the first law of thermodynamics for the time evolution of its total internal energy $E(t)$, including a sink term $L(t)$ for the luminosity radiated from the shell surface:

$$\frac{\mathrm{d}E}{\mathrm{d}t} = \dot{E} = -4\pi R_{\mathrm{s}}^2(t)P(t)v_{\mathrm{s}}(t) - L(t)\,. \tag{H1}$$

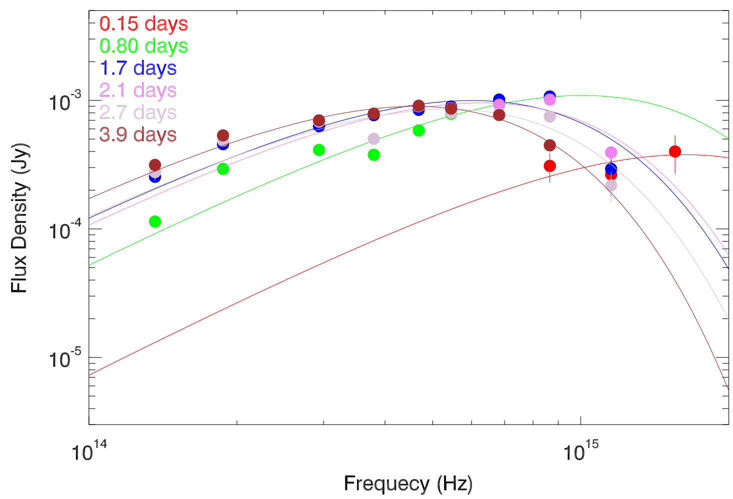

FIG. 18.— SED fit of the early UVOIR data of SN 2008D. The last epoch already begins to show a strong contribution of the SN.

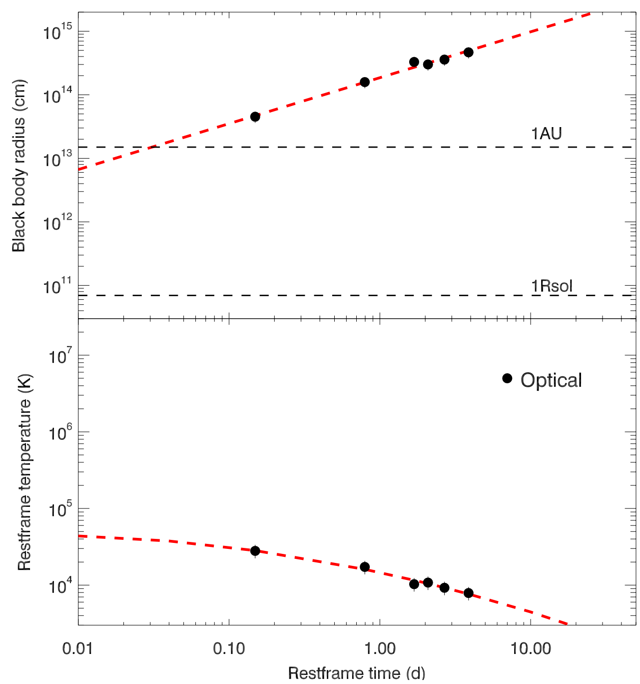

FIG. 19.— Temporal evolution of the radius and temperature for the pre-SN epochs of SN 2008D.

The first term represents the pressure-driven expansion (PdV-) work done by the shell. The shell radius $R_{\rm s}(t) = R_{\rm s,0}(t/t_0)^x$ is assumed to follow a power-law increase with time t as observed, and $v_{\rm s}(t) = \dot{R}_{\rm s}(t)$ is the corresponding expansion velocity. For the conditions of interest the pressure and energy density in the shell of volume $V_{\rm s} = \frac{4\pi}{3}R_{\rm s}^3$ are radiation dominated (this is an excellent approximation throughout the considered evolution), in which case the pressure is given by $P \approx \frac{1}{3}E/V_{\rm s} = \frac{1}{4\pi}E/R_{\rm s}^3$. For estimating the luminosity we adopt the diffusion approximation, which gives $L \approx E/t_{\rm d}$ with the diffusion timescale being $t_{\rm d} = \xi\kappa M_{\rm s}/(cR_{\rm s})$, when $M_{\rm s}$ is the mass of the radiating shell, $\kappa = 0.40 f_e\,{\rm cm^2 g^{-1}}$ is the Thompson opacity for the scattering of photons by free electrons (we choose $f_e = 0.875$ for the number of free electrons per baryon, corresponding to a fully ionized mix of 75% hydrogen and 25% helium), c is the speed of light, and ξ is a numerical factor that accounts for deviations of the detailed geometry and structure from a homogeneous sphere (following Arnett et al. 1980 and Kulkarni et al 2005 we adopt $\xi = 0.07$). Putting all together, Eq. (H1) becomes

$$\frac{\dot{E}}{E} = -\frac{1}{t_{\rm d}(t)} - \frac{x}{t}\,. \tag{H2}$$

Using the observed power-law growth of $R_s(t)$, Eq. (H2) can be solved to yield

$$E(t) = E_0 \left(\frac{t_0}{t}\right)^x \exp\left(-\frac{t^{x+1} - t_0^{x+1}}{(x+1)t_{d,0}t_0^x}\right) , \tag{H3}$$

where $t_{d,0} = t_d(0)$. The first time-dependent factor describes the decrease of $E(t)$ due to the expansion work, the exponential factor results from the radiation cooling. Given $E(t)$, the temperature evolution $T(t)$ can be computed by using $E(t) = aT^4(t)V_s(t)$ with the radiation constant $a = 7.56 \times 10^{-15}\,\mathrm{erg\,cm^{-3}K^{-4}}$.

The results for $T(t)$ for different choices of model parameters (in all cases taking $R_{s,0} = 2 \times 10^{14}$ cm at $t_0 = 0.01$ d) are plotted in the Figure and follow the time-dependence $T(t) \propto (t_0/t)^x \exp(-Y(t)/4)$, where $Y(t)$ is the absolute value of the exponent of the exponential function in Eq. (H3). While the early T-decline is governed by the growth of $R_s(t)$, the steeper decrease of the temperature at late times is caused by the exponential factor associated with radiation losses. Good agreement between model results and observational data can be achieved when a shell mass of $M_s = 0.05$–$0.1\,M_\odot$ and an initial thermal energy of $E_0 = (1$–$2)\times 10^{49}$ erg are assumed.

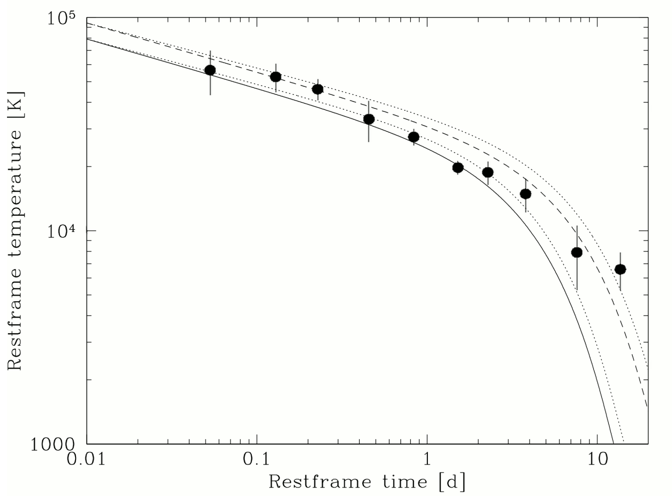

FIG. 20.— Temperature evolution of a gas sphere (or radially extended shell) that cools because of expansion and radiation losses. The sphere radius is assumed to increase according to a power law t^x with $x = 0.23$ (solid and lower dotted curves) or $x = 0.21$ (dashed and upper dotted curves) as observed. The lower pair of lines was computed with an ejecta mass of $0.05\,M_\odot$ and an initial thermal energy of 10^{49} erg, the upper pair of lines with $0.10\,M_\odot$ and 2×10^{49} erg. The curves bracket the observational data points. After more than 10 days electron recombination can no longer be ignored (as in the model) and deviations between the measured data and the model predictions begin to emerge.

To determine the geometry of the CE ejecta and the agreement of our model with the observations of the UVOIR BB emission, we test two extreme geometries of the ejecta: a spherical shell with inner, outer radii of 2×10^{14} and 3×10^{14} cm respectively, and a torus with distance 3×10^{14} cm and tube radius 10^{14} cm. We take an X-ray source of $6 \times 10^{47}\,\mathrm{erg\,s^{-1}}$ lasting for 1000 s. The shell absorbs all of the X-ray emission and the temperatures produced are $> 100,000$ K ($E_{\mathrm{X-ray}} = aT^4V$ where a is the radiation constant, T is the ejecta temperature and V is the ejecta volume). Our torus simulations with the same X-ray source produces a peak temperature in the ejecta of $17,000$ K, since a large part of the X-rays are reflected.

To explain the initial $\sim 40,000$ K temperatures derived from the UVOIR BB emission, the true geometry lies between those two cases, well within what we expect from common envelope ejecta. Assuming that the duration of the UVOIR emission is comparable to the diffusion time of the ejecta, we can also determine its density and find for our two geometrical models a value of around $10^{-11}\mathrm{g\,cm^{-3}}$.

REFERENCES

Anupama, G. C., et al. 2001, A&A, 367, 506
Arntett, W. D. 1980, ApJ, 237, 541
Barkov, M. V., & Komissarov, S. S., 2010, MNRAS, submitted (arXiv:1012.4565v2)
Bloom, J. S., et al. 2009, ApJ, 691, 723
Breeveld, A. A., et al. 2010, MNRAS, 406, 1687
Campana, S., et al. 2006, Nature, 442, 1008
Campana, S., et al. 2010, GCN Circ. 11501
Cano, Z., et al. 2011, MNRAS, 413, 669
Cenko, S. B. 2010, GCN Circ. 11506
Cummings, J. R., & Sakamoto, T. et al. 2010, GCN Circ. 11504
Fassia, A., et al. 2001, MNRAS, 325, 907
Ferrero, P., et al. 2006, A&A, 457, 857
Frail, D. A. 2011, GCN Circ. 11550
Fryer, C. L., & Woosley, S. E., 1998, ApJ, 502, L9
Fynbo, J. P. U., & Xu, D. 2011, GCN Circ. 11563
Galama, T. J., et al., 1998, Nature, 395, 670
Gaskell, C. M. 1992, ApJ, 389, L17
Gehrels, N., et al. 2004, ApJ, 611, 1005
Holland, S. T., et al. 2010, ApJ, 717, 223
Jester, S., et al. 2005, AJ, 130, 873
Kann, D. A., Klose, S., & Zeh, A. 2006, ApJ, 641, 993
Kann, D. A., et al., 2010, ApJ, 720, 1536
Kann, D. A., et al. 2011, ApJ, in press (arXiv:0804.1959v2)
Kulkarni, S. R. 2005, arXiv:astro-ph/0510256
Kulkarni, S. R., et al. 1998, Nature, 395, 663

Lentz, E. J., et al. 2001, ApJ, 547, 506
Leonard, D. C., et al. 2002, PASP, 114, 35
Mazzali, P., et al., 2006, Nature, 442, 1018
Oke, J. B., et al. 1995, PASP, 107, 375
Palmer, D. M., et al. 2010, GCN Circ. 11500
Pian, E., et al., 2006, Nature, 442, 1011
Poole, T. S., et al. 2008, MNRAS, 383, 627
Racusin, J. L., et al. 2010, GCN Circ. 11493
Richardson, J. C., et al. 2011, ApJ, in press (arXiv:1102.2902)
Richmond, M. W., et al. 1996, AJ, 111, 327
Roming, P. W. A., et al. 2009, ApJ, 690, 163
Sakamoto, T., et al. 2010, American Institute of Physics Conference Series, 1279, 20
Serino, M., et al. 2010, GCN Circ. 11505
Soderberg, A., et al., 2006, ApJ, 636, 391
Soderberg, A., et al., 2008, Nature, 453, 469
Sollerman, J., et al. 2007, A&A, 466, 839
Starling, R. L. C., et al., 2011, MNRAS, 411, 2792
Stritzinger, M., et al. 2002, AJ, 124, 2100
Tanvir, N. R., et al. 2011, GCN Circ. 11564
Verner, D. A., et al. 1996, ApJ, 465, 487
Wiersema, K., et al., 2007, A&A, 464, 529
Wiersema, K., et al. 2008, A&A, 481, 319
Wiersema, K., Tanvir, N. R., & Levan, A. J. 2010, GCN Circ. 11502
Wilms, J., Allen, A., & McCray, R. 2000, ApJ, 542, 914
Woosley, S. E., & Bloom, 2006, ARA&A, 44, 507
Xu, D., Ilyin, I., & Fynbo, J. P. U. 2010, GCN Circ. 11495
Xu, D., Ilyin, I., & Fynbo, J. P. U. 2010, GCN Circ. 11496
Xu, D., Hakala, P., & Fynbo, J. P. U. 2010, GCN Circ. 11508
Xu, D., et al. 2011, GCN Circ. 11519
Zauderer, A., Berger, E., & Fong, W. 2011, GCN Circ. 11770
Zeh, A., Klose, S., & Hartmann, D. H. 2004, ApJ, 609, 952
Zhang, W., & Fryer, C. L., 2001, ApJ, 550, 357
Zhang, B., & Mészáros, P., 2004, Internat. Journal of Modern Physics A, 19, 2385